

Nonequilibrium Molecular Dynamics, Fractal Phase-Space Distributions, the Cantor Set, and Puzzles Involving Information Dimensions for Two Compressible Baker Maps.

William Graham Hoover and Carol Griswold Hoover

Ruby Valley Research Institute

Highway Contract 60, Box 601

Ruby Valley, NV 8983

(Dated: December 21, 2024)

Abstract

Deterministic and time-reversible nonequilibrium molecular dynamics simulations typically generate “fractal” [fractional-dimensional] phase-space distributions. Because these distributions and their time-reversed twins have zero phase volume, stable attractors “forward in time” and unstable (unobservable) repellers when reversed, these simulations are consistent with the Second Law of Thermodynamics. These same reversibility and stability properties can also be found in compressible Baker Maps, or in their equivalent random walks, motivating their careful study. We illustrate these ideas with three examples: a Cantor-Set Map and two linear compressible Baker Maps, $N2(q,p)$ and $N3(q,p)$. The two Baker Maps’ Information dimensions estimated from sequential mappings agree while those from pointwise iteration do not, with the estimates dependent upon details of the approach to the maps’ nonequilibrium steady states.

Keywords: Chaos, Lyapunov Exponents, Irreversibility, Random Walks, Maps, Information Dimension

I. NONEQUILIBRIUM MOLECULAR DYNAMICS GENERATES FRACTALS

The computers developed for the National Laboratories were first applied to manybody problems in the 1950s. At Los Alamos in 1953, Fermi, Pasta, and Ulam¹ described the incomplete equilibration of one-dimensional waves in anharmonic chains. Soon afterward, at Livermore, Berni Alder and Tom Wainwright simulated the motion of systems of several hundred hard disks and spheres². At Brookhaven George Vineyard and his coworkers studied “realistic” atomistic models of the impact of high-energy radiation on models of simple metals shortly thereafter³. All of these atomistic simulations were developed based on classical Newtonian mechanics with short-ranged pairwise-additive forces. “Large” simulations involved several hundred discrete particles. A generation later simulations with millions of particles were possible. **Figure 1** shows a typical simulation from our 1989-1990 visit to Japan. These indentations of amorphous Stillinger-Weber silicon, using two different indenter models, generate plastic flow near the indentors⁴. Trillion-atom simulations are feasible in 2020.

In 1984 Shuichi Nosé had announced a revolutionary method for imposing specified temperatures and pressures on molecular dynamics simulations^{5,6}. His modification of Hamiltonian mechanics was designed to replicate Gibbs’ isothermal and isobaric ensembles. Equilibrium distributions had been formulated by Gibbs’ statistical mechanics prior to the close of the 19th century. To match Gibbs’ results Nosé found it necessary to introduce a “scaled” time which had the drawback of introducing wild fluctuations in the dynamics. Hoover helped develop these ideas into practical numerical algorithms⁷ which avoided time-scaling. The simplest problem to which the Nosé-Hoover approach can be applied is the harmonic oscillator with unit mass, force constant, and temperature :

$$\dot{q} = p ; \dot{p} = -q - \zeta p ; \dot{\zeta} = p^2 - 1 \text{ [NH]} .$$

Here (q, p) are the oscillator coordinate and momentum. The time-averaged kinetic temperature, $\langle p^2 \rangle$ is controlled (“thermostatted”) by the time-reversible friction coefficient ζ . The reader can verify, as was pointed out in Reference 7, that applying the steady-state continuity equation for the flow in (q, p, ζ) space gives Gibbs’ canonical distribution for the

oscillator together with a Gaussian distribution for the friction coefficient ζ :

$$(\partial f / \partial t) = 0 = -\partial(f\dot{q})/\partial q - \partial(f\dot{p})/\partial p - \partial(f\dot{\zeta})/\partial \zeta \longleftrightarrow f(q, p, \zeta) \propto e^{-(q^2+p^2+\zeta^2)/2} .$$

This idea and its isobaric analog have become standard approaches to equilibrium molecular dynamics simulations for a wide variety of systems both large and small.

Although pairwise-additive potentials might seem an oversimplification, work earning Nobel Prizes in chemistry (1986 and 2013), carried out by Dudley Herschbach and Martin Karplus and their colleagues, showed otherwise⁸. Straightforward classical solutions of pairwise-additive motion turned out to be quite useful in interpreting and predicting the properties of molecules both simple (hydrogen and various alkali halides) and complex (proteins). In most isoenergetic dynamics simulations atomistic trajectories are generated using the “Verlet” or “Störmer” algorithm, with its roots going all the way back to Newton. This algorithm expresses the “next” coordinate value, x_{t+dt} in terms of the previous and current coordinates along with the current value of the acceleration \ddot{x}_t :

$$x_{t+dt} = 2x_t - x_{t-dt} \equiv dt^2(F_x/m)_t \longleftarrow \ddot{x} = (F_x/m) .$$

Similar time-reversible algorithms have been developed for isothermal and isobaric systems⁹.

Though not time-reversible, fourth-order Runge-Kutta integration of the system of first-order motion equations,

$$\{ \dot{x} = (p_x/m) ; \dot{p}_x = F_x \} ,$$

provides better accuracy at a fixed timestep dt , particularly for the velocities. Typical equilibrium simulations, based on Newtonian or Hamiltonian or Nosé-Hoover mechanics, use periodic boundary conditions. Series of such simulations can be used to generate “equations of state”, temperature and pressure as functions of energy and density.

Nonequilibrium simulations such as Vineyard’s radiation-damage studies, or the simulation of planar shockwaves, require the implementation of special boundary conditions capable of imposing velocity and temperature differences across systems of interest. An early discovery motivating quantitative atomistic simulations was the finding that the width of strong shockwaves is on the order of the size of molecules so that details can be modelled reasonably well with only a few thousand particles. The atomistic and continuum

descriptions of strong shockwaves were in rough, ten percent, agreement with one another¹⁰.

By 1987 a significant difference between equilibrium and nonequilibrium steady states had come to light. Simple nonequilibrium simulations were shown to produce fractal (fractional-dimensional) phase-space distributions, with a negligible phase-space volume relative to corresponding higher-dimensional equilibrium Gibbs' distributions, such as the microcanonical and canonical ensembles^{11–13}. About the simplest steady-state mechanical problem results when heat is driven through a Nosé-Hoover harmonic oscillator exposed to a temperature gradient^{14,15}. Where the maximum value of the temperature gradient is ϵ the three motion equations (for the coordinate q , the momentum p , and the current-driving friction coefficient ζ), are as follows :

$$\dot{q} = p ; \dot{p} = -q - \zeta p ; \dot{\zeta} = p^2 - T(q) ; T(q) = 1 + \epsilon \tanh(q) [\text{NH}] .$$

Here again, the oscillator mass, force constant, and mean temperature have all been chosen equal to unity, but the temperature gradient can generate nonequilibrium steady states. The three coupled equations give rise to a wide variety of solutions. Three such solutions, all for a maximum temperature gradient $\epsilon = 0.42$, are shown in **Figure 2**. There we see a dissipative limit cycle as well as two conservative tori. Chaotic solutions are also accessible to the model. More complicated mechanical models, with two friction coefficients, ζ and ξ , and the same coordinate dependence of the temperature, $T(q) = 1 + \epsilon \tanh(q)$, can generate *ergodic* fractal distributions. In ergodic systems the same longtime steady-state solutions obtained apply for any initial condition (“almost any” for the mathematically minded). Two examples are shown in **Figure 3**. The Hoover-Holian¹⁶ and Martyna-Klein-Tuckerman¹⁷ motion equations which generated them are as follows :

$$\dot{q} = p ; \dot{p} = -q - \zeta p - \xi p^3 ; \dot{\zeta} = p^2 - T(q) ; \dot{\xi} = p^4 - 3p^2 T(q) ; [\text{HH}] ;$$

$$\dot{q} = p ; \dot{p} = -q - \zeta p ; \dot{\zeta} = p^2 - T(q) - \xi \zeta ; \dot{\xi} = \zeta^2 - T(q) ; [\text{MKT}] .$$

At equilibrium, with $T \equiv 1$, the two Hoover-Holian thermostat variables control both the second and the fourth moments of momentum. The Martyna-Klein-Tuckerman ξ controls the distribution of the other thermostat variable ζ . Detailed investigations of these oscillator problems at equilibrium show that both the HH and the MKT dynamics give the same

ergodic distribution, including Gibbs' canonical Gaussians in both q and p .

$$f(q, p, \zeta, \xi) \propto e^{-(q^2+p^2+\zeta^2+\xi^2)/2}.$$

The distributions away from equilibrium can be qualitatively different! The fractal ergodic nature of nonequilibrium states generated with a variable $T(q)$ provides a simple explanation for the irreversible behavior (despite time-reversible motion equations) described by the Second Law of Thermodynamics. When the nonequilibrium motion equations are solved, the fractal strange attractor states which result are not only vanishingly rare. In addition their time-reversed states (with the momenta and the friction coefficients' signs changed) describe mechanically-unstable fractal repellers. Because such repellers correspond to *exploding* rather than *collapsing* phase-space objects they are *unobservable*, having negative transport coefficients and entailing entropy destruction rather than production!¹¹⁻¹³.

From a thermodynamic standpoint phase-volume increase corresponds to heating and decrease to cooling. Because irreversible processes necessarily increase heat it follows that a stationary nonequilibrium distribution must extract net heat, leading to the formation of a fractal attractor. A reversed process converting heat to work, a repeller, is outlawed by both the Second Law of Thermodynamics and by computational instability in time-reversed numerical simulations¹².

We consider fractal distributions in more detail in the following Sections. We have already seen that in the 1980s nonequilibrium molecular dynamics led to the characterization of fractal (fractional dimensional) distributions. These are qualitatively different to Gibbs' smooth equilibrium distributions. Because the mathematics of fractals and their geometric characterization is interesting and sometimes paradoxical we highlight stimulating research areas well-suited to student exploration in what follows. In Section II we begin with the simplest fractal, the Cantor set, and a description of its fractal dimensionality. Section III takes up time-reversible compressible Baker Maps, where phase-volume changes model nonequilibrium heat transfer. The one-way nature of these maps ("Time's Arrow") is a direct geometric analog of the Second Law conversion of work to heat. Finally we consider Kaplan and Yorke's relation linking the fractal information dimension to the Lyapunov exponents. We show that their conjectured equality between the information dimension and the Kaplan-Yorke dimension, $D_{KY} \stackrel{?}{=} D_I$, is precisely true for one Baker map, N3, and

apparently false for its very similar twin, N2. This surprise was completely unexpected. It richly deserves further study.

II. THE CANTOR SET AND THE FRACTAL INFORMATION DIMENSION

The simplest fractal is arguably the “Middle-Third” “Cantor Set”. The Middle-Third description suggests one of the several means for constructing the set: Begin with the unit interval $[0 \text{ to } 1]$; Discard the middle third $[(1/3 \text{ to } (2/3)]$ leaving two intervals, $[(0/3 \text{ to } (1/3)]$ and $[(2/3 \text{ to } (3/3)]$; Discard the middle third of those two, leaving four intervals of length $(1/9)$; Finally, imagine the limiting set of points remaining after an infinite number (\aleph_0 , the number of integers) of removal stages.

A more elegant alternative description of this same Cantor Set, or “Cantor Dust”, is the set of numbers on the unit interval whose ternary representation is composed wholly of 0s and 2s. An example set member is the base-3 number $0.20220000\dots = 2/3 + 0/9 + 2/27 + 2/81 + 0 = 62/81$. Because each of \aleph_0 digits of the Cantor set can be either a 0 or a 2 the (likewise infinite) number of Cantor-Set members is $2^{\aleph_0} \equiv \aleph_1$. The fact that the continuum itself, when expressed in binary base-2 rather than ternary base-3, has likewise \aleph_1 members, all the binary combinations of 0s and 1s, seems paradoxical. The continuum has no holes while the well-named Cantor Dust has nothing but! Does it really make “sense” to accept the notion that the members of the continuum and the Cantor Set are equinumerous? Worse still – how sound is the notion that the number of members of the continuum is invariably \aleph_1 , independent of the continuum’s dimensionality, one, two, three, ...? These troubling counter-intuitive aspects of Cantor’s ideas (and the undecidability of the Continuum Hypothesis) suggest an aesthetic-but-inapplicable branch of mathematics. Nevertheless let us pursue a descriptive approach to dimensionality differences among the various infinite fractal subsets of continua.

Alfréd Rényi described recipes for various fractal dimensions long ago, the fractal dimension, information dimension, correlation dimension. Expressed in terms of the probabilities $\{ p \}$ of occupying a set of bins, all of the same size δ , with δ sufficiently small, the forms of these three are as follows:

$$D_0 = \ln(\sum[p^0]) / \ln(1/\delta) ; D_1 = \sum[p \ln p] / \ln(\delta) ; D_2 = \ln(\sum[p^2]) / \ln(\delta) .$$

The sums include all occupied bins. The probabilities are normalized, $\sum[p] \equiv 1$, and are typically proportional to the number of counts or the fractions of the total time associated with residence in each of the occupied bins. The fractal (or capacity), information, and correlation dimension correspond to D_0 , D_1 , and D_2 . The reader can verify that in the case of the Cantor set these three dimensions are all the same, $D = \ln(2)/\ln(3) = 0.630930$. Notice that reducing the bin size by a factor of three results in just twice as many occupied bins. Likewise, coarsening the bin size by a factor of three results in just half as many occupied bins. D plays the role of a (fractional) dimension: $3^D = 2 \longleftrightarrow D = \ln(2)/\ln(3)$.

This simplest of fractals sets the stage for studying two interrelated families of nonequilibrium fractals even simpler than those generated by the conducting harmonic oscillator problems. The two families of simpler models are [1] stochastic random walks (usually on the unit interval from 0 to 1) and [2] deterministic time-reversible compressible maps (where we use a rotated 2×2 diamond-shaped domain in order to model time-reversibility and to enhance ergodicity). The expected equivalence of these models is itself interesting. The fact that such simple models can lead to results that are contradictory or paradoxical, despite the long history of their study, is currently in need of further pedagogical explanation. The Ian Snook Prize for 2020¹⁸, to be awarded to the author(s) best addressing this need, is designed to shed light on these families of fractal problems.

The information dimension $D_I = D_1$, a close relative of Gibbs' statistical entropy, is arguably the most useful descriptor of fractal point sets or distributions. Using the $p \ln p$ formula for $\delta = 1/27$ there are eight three-digit members of the Cantor set :

$$\{ 0.000, 0.002, 0.020, 0.022, 0.200, 0.202, 0.220, 0.222 \} .$$

The resulting dimensionality is $\ln(1/8)/\ln(1/27) = \ln(2)/\ln(3) = 0.630930$. For any fixed number of digits the same distribution-based result is obtained. A numerical representation of the Cantor set as an arbitrarily-large set of points can be generated by choosing an initial "seed" in the set, like $C = 2/9$ or $C = 62/81$, followed by iteration of the following loop of FORTRAN pseudocode:

```

call random_number(R)
if(R.lt.0.5) Cnew = (C/3)
if(R.ge.0.5) Cnew = (C/3) + (2/3)
C = Cnew
write(33,*) it,C
[ Unit Square Generation of the Cantor Set in (R,C) Cartesian Coordinates ]

```

Here the FORTRAN `random_number` subroutine generates series of random numbers $\{ R \}$ uniformly distributed between zero and one. Notice particularly that exactly the same pseudocode describes a random walk with variable length steps. Half the time the walker moves left from his present position C to $C/3$ corresponding to adding a ternary 0 after the “decimal” point. Otherwise, and also half the time, the walker moves to the right, corresponding to adding in a ternary 2 after the point. The overall single-step operation shifts the ternary representation of C one digit to the right and then chooses randomly either 0 or 2 to precede it.

Alternatively, a deterministic two-dimensional compressible map can be constructed to generate the Cantor Set in a rotated (q, p) space with the constant d equal to $\sqrt{2}/6$:

```

if(q.lt.p) qnew = + (7*q)/6 - (5*p)/6 + 5*d
if(q.lt.p) pnew = - (5*q)/6 + (7*p)/6 - 1*d
if(q.ge.p) qnew = + (7*q)/6 - (5*p)/6 - 5*d
if(q.ge.p) pnew = - (5*q)/6 + (7*p)/6 + 1*d
q = qnew
p = pnew
[ Diamond-Shaped Generation of the Cantor Set in (q,p) Space ]

```

100,000 points generated with these stochastic and deterministic mappings are illustrated in Figure 4. Here and in that Figure, just for convenience in the programming, the 2×2 diamond-shaped domain has extreme values of q and p of $\pm\sqrt{2}$. In the next Section we elaborate on our preference for the rotated map of the two-dimensional (q, p) domains rather than the conventional (x, y) unit square.

III. INFORMATION DIMENSIONS FOR COMPRESSIBLE BAKER MAPS

The Baker Map considered by Eberhard Hopf in 1937 provides a simple deterministic model for the dissipative chaos causing irreversible behavior in the solutions of time-reversible motion equations. By 1987 several examples of thermostatted molecular dynamics led to the representation of nonequilibrium steady states as fractal structures in (q, p) (coordinate, momentum) phase space^{11–13}. A two-panel Baker Map N2, incorporating twofold changes in the area $dqdp$ is the prototypical example, displayed in **Figures 5 and 6**. This mapping^{19–22} follows the equations

```

if(q-p.le.-sqrt(2/9)) qnew = + (11/ 6)*q - ( 7/ 6)*p + 14*d
if(q-p.le.-sqrt(2/9)) pnew = - ( 7/ 6)*q + (11/ 6)*p - 10*d
if(q-p.gt.-sqrt(2/9)) qnew = + (11/12)*q - ( 7/12)*p - 7*d
if(q-p.gt.-sqrt(2/9)) pnew = - ( 7/12)*q + (11/12)*p - 1*d
[ Nonequilibrium Two-Panel Baker Map N2 ]

```

where the constant d is $\sqrt{1/72}$. The map is irrotational, with unstable fixed points at the top and bottom of the diamond-shaped domain where q is horizontal and p vertical. The diamond-shaped domain used here, $-\sqrt{2} < q, p < +\sqrt{2}$, is purposefully rotated 45 degrees from the usual Cartesian Baker Map. So as to emphasize the time-reversibility of our compressible Baker Map N2 we choose the diamond-shaped 2×2 domain. Reversing the time corresponds to reversing the sign of the (vertical) “momentum” p while keeping the horizontal “coordinate” q unchanged.

This Nonequilibrium Baker Map N2 is “time-reversible” in the sense that the inverse mapping, $N2^{-1}$ is given by the product mapping $T*N2*T$. The time-reversal mapping T simply changes the sign of the momentum, $T(q, \pm p) = (q, \mp p) = T^{-1}(q, \pm p)$. A typical long-time cumulative solution of the N2 mapping is far from homogeneous but is nonetheless ergodic, with nonvanishing density everywhere within its diamond-shaped domain. This nonequilibrium (area-changing) mapping produces no “holes” so that its capacity or box-counting or fractal dimension is 2. See the 100,000-point samples of the mapping and its inverse in **Figure 5**. The N2 mapping is compressive parallel to the line $q = p$ and expansive in the perpendicular direction. Numerical work indicates that the resulting distribution of points is random in \tilde{x} and remains fractal in \tilde{y} where the orthogonal coordinates (\tilde{x}, \tilde{y}) occupy

a 2×2 square centered on the origin :

$$-1 < \tilde{x} = (q - p)/\sqrt{2} ; \tilde{y} = (q + p)/\sqrt{2} < +1 .$$

For convenience in the measurement of the fractal information and correlation dimensions and the construction of random walks in y corresponding to the fractal direction parallel to $q = p$, it is convenient to map the 2×2 (\tilde{x}, \tilde{y}) square onto the unit (x, y) square :

$$x \equiv (\tilde{x} + 1)/2 ; y \equiv (\tilde{y} + 1)/2 .$$

Then an equivalent set of (x, y) values can be generated by a random walk based on random numbers from the unit interval, $0 < \{ \mathbf{r} \} < +1$ as follows :

```
call random_number(r)
x = r
call random_number(r)
if(r.lt.(2/3)) ynew = (0+1*y)/3
if(r.ge.(2/3)) ynew = (1+2*y)/3
y = ynew
[ Two-Panel Nonequilibrium Random Walk in the Unit Square, N2 ]
```

Because the N2 mapping and this random walk generate the *same* long-time distributions of the compressive y variable the various fractal dimensions²³⁻²⁵ $\{ D \}$ (box-counting, information, Kaplan-Yorke, and correlation, ...) are simply related, $D_{\text{map}}(q, p) = D_{\text{walk}}(y) + 1$.

Careful investigations^{21,22} of the local densities of points in two-dimensional bins of area $\delta^2 = (1/3)^{2M}$, with the integer M up to 20, suggested a pointwise fractal information dimension of 1.741₅. But mapping *regions* rather than *points*, and starting with a uniform distribution in the diamond-shaped domain gave a totally different result ! The information dimension calculated for the same N2 map according to the mapping of regions (areas) rather than by propagation of a single mapped point can be calculated analytically²⁴. The result is $D_{\text{regions}}^{\text{N2}} = 1.789690$ rather than $D_{\text{points}}^{\text{N2}} = 1.741_5$.

A. The Kaplan-Yorke Dimension from Lyapunov Instability

On the other hand – forty years ago – Kaplan and Yorke²⁶ conjectured that the fractal information dimensions of solutions of typical two-dimensional maps are simply related to the solutions’ Lyapunov exponents. Because two-thirds of the N2-mapped area undergoes a 1.5-fold stretching while one-third undergoes three-fold stretching the larger Lyapunov exponent is $\lambda_1 = (2/3) \ln(3/2) + (1/3) \ln(3) = +0.636514$. The smaller (negative) Lyapunov exponent describes the shrinking: $\lambda_2 = (2/3) \ln(1/3) + (1/3) \ln(2/3) = -0.867563$. Kaplan and Yorke reasoned that the information dimension for such a map is given by

$$D_I = 1 - (\lambda_1/\lambda_2) = 1.733680 ,$$

a bit less than the estimate from bin-density data^{21,22} and far from the analytic area-mapping result, 1.789690.

In our efforts to understand these differences we came upon a related N3 mapping, compared to N2 in **Figure 6**. N3 is a slight elaboration of N2, and from the standpoint of irrotational area mappings produces the same information dimension. Here is the FORTRAN description of a single step in the corresponding Random Walk :

```
call random_number(r)
x = r
call random_number(r)
if (r.lt.(2/3))                ynew = (y/3) + (0/3)
if((r.ge.(2/3)).and.(r.le.(5/6))) ynew = (y/3) + (1/3)
if (r.gt.(5/6))                ynew = (y/3) + (2/3)
y = ynew
[ Three-Panel Nonequilibrium Random Walk, N3 ]
```

Throughout our numerical work we have used the handy FORTRAN random-number generator indicated here, “`random_number(r)`”, said to have a repeat length of order 10^{77} (!)

To illustrate the differences in ordering of the bin populations resulting from the first four steps of the random walks equivalent to N2 and N3 we compare million-point 81-bin histograms of the two Walks in **Figures 7 and 8**. Evidently the N3 mapping, starting with a uniform distribution, produces exactly the same set of bin probabilities as does N2 (though

in a different order) and so the walks have exactly the same information dimensions²⁴, 0.789690. But in the N3 case the Lyapunov exponents, and the Kaplan-Yorke dimension, are different, and produce an interesting surprise :

$$\lambda_1 = (2/3) \ln(3/2) + (1/3) \ln(6) = 0.867563 ; \lambda_2 = (2/3) \ln(1/3) + (1/3) \ln(1/3) = -1.098612 .$$

$$\rightarrow D_{KY} = 1 - (\lambda_1/\lambda_2) = 1.789690 . \text{ [Equivalent to } D_I \text{ for N3]} .$$

In fact *this time* the Kaplan-Yorke conjecture is true, provided one imagines that the steady state maintains the stationary value of the information dimension observed during the evolution suggested by **Figure 9** ! A proof or disproof of this thought would be welcome.

IV. DISCUSSION AND CONCLUSIONS

The Kaplan-Yorke conjecture $D_I \stackrel{?}{=} D_{KY}$ is forty years old. It is surprising that the apparent counterexample for the linear N2 mapping considered here evaded detection for so many years. We have seen that the generalized Baker Maps N2 and N3 agree with both the thermodynamic and the computational statements of the Second Law of Thermodynamics. The Baker Map fractals provide exactly the same computational mechanism for dissipation as is present in manybody simulations. But our understanding remains incomplete. Why *is* or *is not* the Kaplan-Yorke approximation valid or invalid for linear maps? The puzzling difference between pointwise dimensionality and regionwise dimensionality is likewise unsettling, but is firmly established by our results.

The mathematics of fractal sets remains paradoxical and challenging. Besides the disagreement between the various versions of the information dimension the simple geometry of fractals is itself puzzling. The popular understanding of cumulus clouds as 2.5-dimensional objects suggests that fractals are isotropic. The Sierpinski carpet and sponge fractals have characteristic rotational symmetries. On the other hand *all* of the fractals arising from statistical mechanics appear to be anisotropic. Particular local directions correspond to exponential instability or stability. Without anisotropy there could be no Kaplan-Yorke analysis of dimension. The unsettling cardinality equivalence of the holy Cantor dust and the holeless continuum, despite their different information dimensions, suggests that there is much more work for the mathematicians to do, perhaps with useful physical applications.

In any event a thorough pedagogical explanation of the situation described here will help to understand these issues. Such an explanation has been set as the 2020 Ian Snook Prize Problem recently described in Reference 18.

V. POSTSCRIPT OF 25 APRIL 2020

We wish to thank the anonymous referee for his many thoughtful suggestions, most of which we have adopted. The abstract has been completely rewritten. Some repetitions and ambiguities have been removed. Our descriptions of the Cantor Set and the geometry of time-reversible maps have both been improved. We decided not to follow the referee's suggestion to add additional references citing work of the many that have been attracted to these and similar problems independently of our own efforts. We believe that any attempt at completeness on our part would have the unintentional effect of slighting others of our kind friends and colleagues. We have chosen to refer here only to those works that have directly influenced our own. Comparing the present version to the arXiv second version of 9 January 2020 will satisfy the curious reader as to all the changes we have made.

-
- ¹ J. Ford, "The Fermi-Pasta-Ulam Problem: Paradox Turns Discovery", *Physics Reports* **213**, 271-310 (1992).
 - ² B. J. Alder and T. E. Wainwright, "Molecules in Motion", *Scientific American* **201**(4), 113-130 (1959).
 - ³ J. B. Gibson, A. N. Goland, M. Milgram, and G. H. Vineyard, "Dynamics of Radiation Damage", *Physical Review* **120**, 1229-1253 (1960).
 - ⁴ W. G. Hoover, A. J. DeGroot, C. G. Hoover, I. Stowers, T. Kawai, B. L. Holian, T. Boku, S. Ihara, and J. Belak, "Large-Scale [millions of atoms] Elastic-Plastic Indentation Simulations *via* Nonequilibrium Molecular Dynamics", *Physical Review A* **42**, 5844-5853 (1990).
 - ⁵ S. Nosé, "A Unified Formulation of the Constant Temperature Molecular Dynamics Methods", *Journal of Chemical Physics* **81**, 511-519 (1984).
 - ⁶ S. Nosé, "A Molecular Dynamics Method for Simulations in the Canonical Ensemble", *Molecular Physics* **100**, 191-198 (2002).

- ⁷ W. G. Hoover, “Canonical Dynamics: Equilibrium Phase-Space Distributions”, *Physical Review A* **31**, 1695-1697 (1985).
- ⁸ M. Karplus, “ ‘Spinach on the Ceiling’ : a Theoretical Chemist’s Return to Biology”, *Annual Review of Biophysics and Biomolecular Structure* **35**, 1-47 (2006).
- ⁹ B. L. Holian, A. J. De Groot, W. G. Hoover, and C. G. Hoover, “Time-Reversible Equilibrium and Nonequilibrium Isothermal-Isobaric Simulations with Centered-Difference Stoermer Algorithms”, *Physical Review A* **41**, 4552-4553 (1990).
- ¹⁰ B. L. Holian, W. G. Hoover, B. Moran, and G. K. Straub, “Shockwave Structure *via* Nonequilibrium Molecular Dynamics and Navier-Stokes Continuum Mechanics”, *Physical Review A* **22**, 2798-2808 (1980).
- ¹¹ B. Moran, W. G. Hoover, and S. Bestiale, “Diffusion in a Periodic Lorentz Gas”, *Journal of Statistical Physics* **48**, 709-726 (1987).
- ¹² B. L. Holian, W. G. Hoover, and H. A. Posch, “Resolution of Loschmidt’s Paradox: The Origin of Irreversible Behavior in Reversible Atomistic Dynamics”, *Physical Review Letters* **59**, 10-13 (1987).
- ¹³ W. G. Hoover, H. A. Posch, B. L. Holian, M. J. Gillan, M. Mareschal, and C. Massobrio, “Dissipative Irreversibility from Nosé’s Reversible Mechanics”, *Molecular Simulation* **1**, 79-86 (1987).
- ¹⁴ H. A. Posch and W. G. Hoover “Time-Reversible Dissipative Attractors in Three and Four Phase-Space Dimensions”, *Physical Review E* **55**, 6803-6810 (1997).
- ¹⁵ J. C. Sprott, W. G. Hoover, and C. G. Hoover, “Heat Conduction, and the Lack Thereof, in Time-Reversible Dynamical Systems. Generalized Nosé-Hoover Oscillators with a Temperature Gradient”, *Physical Review E* **89**, 042914 (2014).
- ¹⁶ W. G. Hoover and B. L. Holian, “Kinetic Moments Method for the Canonical Ensemble Distribution”, *Physics Letters A* **211**, 253-257 (1996).
- ¹⁷ C. J. Martyna, M. L. Klein, and M. Tuckerman, “Nosé-Hoover Chain—the Canonical Ensemble *via* Continuous Dynamics”, *Journal of Chemical Physics* **97**, 2635-2643 (1992).
- ¹⁸ W. G. Hoover and C. G. Hoover, “2020 Ian Snook Prize Problem: Three Routes to the Information Dimensions for One-Dimensional Stochastic Random Walks and Their Equivalent Two-Dimensional Baker Maps”, *Computational Methods in Science and Technology* **25**, 153-159 (2019).

- ¹⁹ W. G. Hoover and H. A. Posch, “Chaos and Irreversibility in Simple Model Systems”, *Chaos* **8**, 366-373 (1998)
- ²⁰ J. Kumičák, “Irreversibility in a Simple Reversible Model”, *Physical Review E* **71**, 016115 (2005).
- ²¹ W. G. Hoover and C. G. Hoover, “Aspects of Dynamical Simulations, Emphasizing Nosé and Nosé-Hoover Dynamics and the Compressible Baker Map”, *Computational Methods in Science and Technology* **25**, 125-141 (2019).
- ²² W. G. Hoover and C. G. Hoover, “Random Walk Equivalence to the Compressible Baker Map and the Kaplan-Yorke Approximation to Its Information Dimension”, arXiv:1909.04526 (2019).
- ²³ C. Grebogi, E. Ott, and J. A. Yorke, “Roundoff-Induced Periodicity and the Correlation Dimension of Chaotic Attractors”, *Physical Review A* **38**, 3688-3692 (1988).
- ²⁴ J. D. Farmer, “Information Dimension and the Probabilistic Structure of Chaos”, *Zeitschrift für Naturforschung* **37 A**, 1304-1325 (1982).
- ²⁵ J. D. Farmer, E. Ott, and J. A. Yorke, “The Dimension of Chaotic Attractors”, *Physica* **7D**, 153-180 (1983).
- ²⁶ J. L. Kaplan and J. A. Yorke, “Chaotic Behavior of Multidimensional Difference Equations”, pages 204-227 in *Functional Differential Equations and the Approximation of Fixed Points*, edited by H. O. Peitgen and H. O. Walther (Springer, Berlin, 1979).

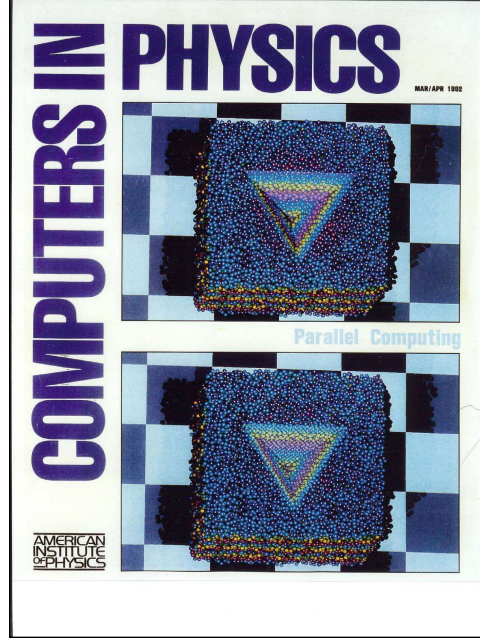


FIG. 1: This 1992 cover illustrates two 32 768-atom indentations of amorphous silicon, one with a smooth-faced tetrahedral indenter, the other with a rough face-centered-cubic atomistic indenter. See Reference 4 for the details. By 2020 simulations with trillions of atoms became feasible.

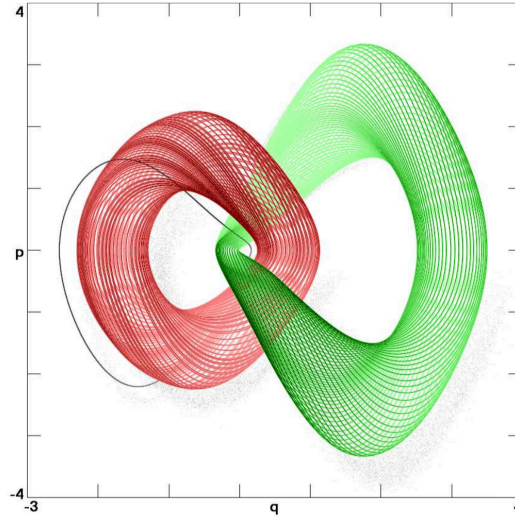


FIG. 2: Three stationary solutions for the Nosé-Hoover oscillator with maximum temperature gradient $\epsilon = 0.42$. Unlike the Borromean rings each of the three solutions here is linked to the other two. See Reference 15 for more details. The two tori are produced using the initial conditions $(q, p, \zeta) = (-2.3, 0, 0)$ and $(3.5, 0, 0)$. The limit cycle is produced using the initial condition $(-2.7, 0, 0)$.

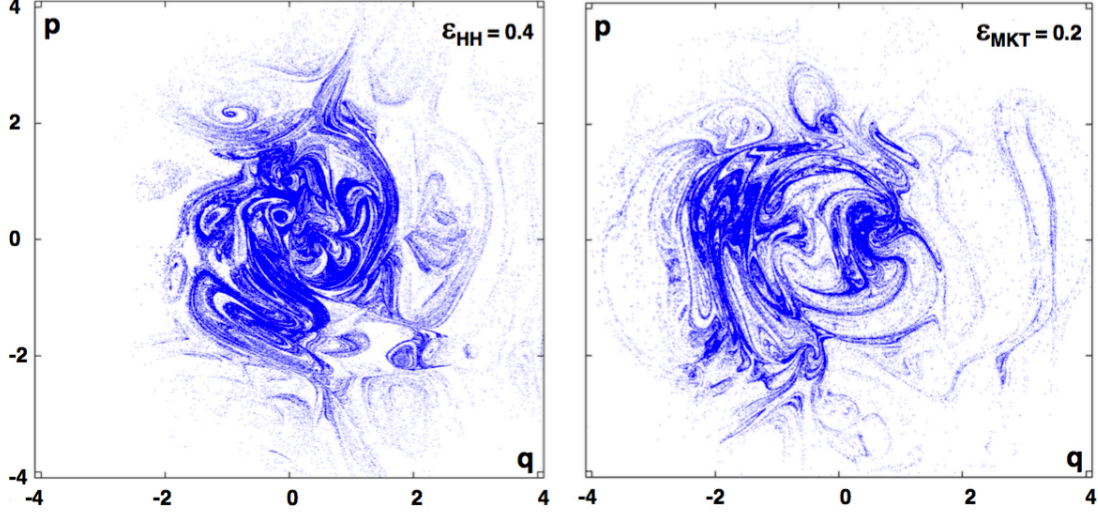


FIG. 3: Two fractal $p(q)$ sections near the $\zeta = \xi = 0$ plane for [left] the Hoover-Holian Oscillator with $\epsilon = 0.40$ and for [right] the Martyna-Klein-Tuckerman Oscillator with $\epsilon = 0.20$. See Section 5.7.2 of W. G. Hoover and C. G. Hoover's *Simulation and Control of Chaotic Nonequilibrium Systems* (World Scientific, Singapore, 2015). The initial conditions are $(q, p, \zeta, \xi) = (1, 0, 0, 0)$ with every fourth-order Runge-Kutta point plotted satisfying $\zeta^2 + \xi^2 < 0.00001$. Both sections were generated with 2×10^{11} timesteps using $dt = 0.003$.

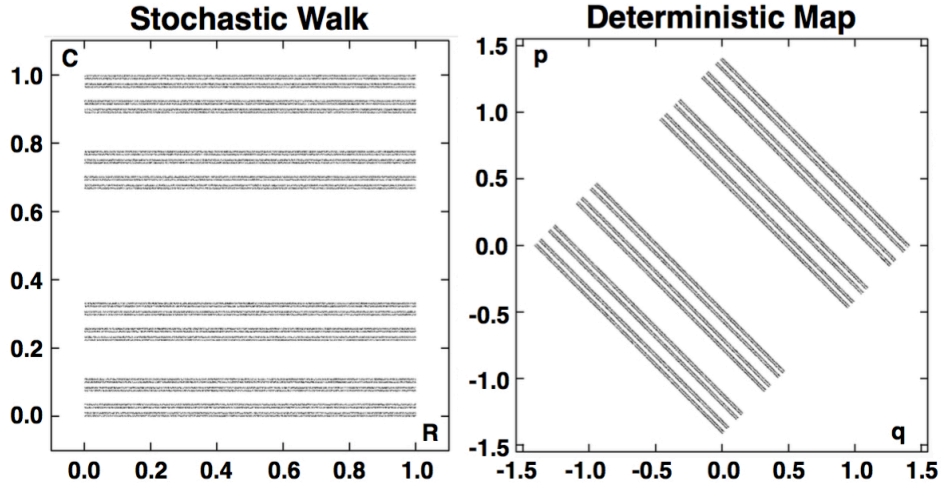


FIG. 4: Two two-dimensional forms of the one-dimensional Cantor Set are shown here. At the left, in the unit square with $0 < R, C < 1$ R is chosen randomly and the C coordinate follows a stochastic random walk governed by R . At the right, in the rotated 2×2 diamond-shaped domain the next (q, p) point follows from the last according to the “Diamond-Shaped Generation” algorithm given at the end of Section II. The Figure shows a sequence of 100,000 points in both cases.

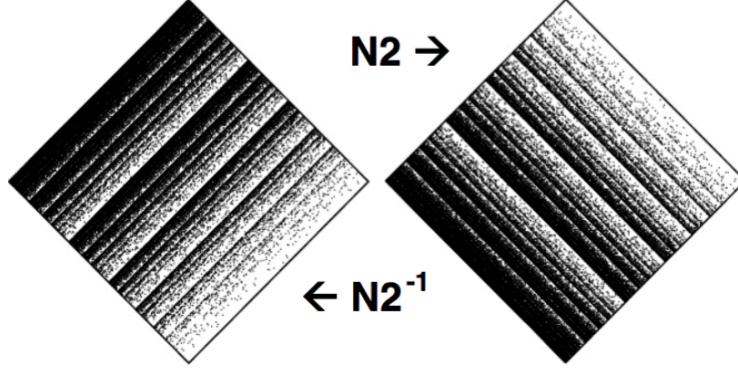


FIG. 5: The repeller generated by $N2^{-1}$ (at left) and attractor generated by $N2$ (at right) using 100 000 iterations from the initial point $(q, p) = (0, 0)$. Note that $-\sqrt{2} < q, p < +\sqrt{2}$. The map is time-reversible so that the repeller is the mirror-image (with the mirror horizontal) of the attractor. Although the fractal dimensions of the attractor and repeller are identical their stabilities (as given by their Lyapunov exponents from $N2$) are opposite as a consequence of their time-reversibility.

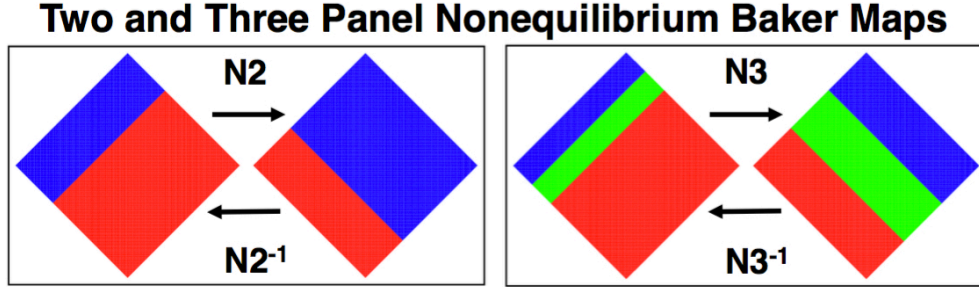


FIG. 6: The rotationless two-panel and three-panel maps $N2$ and $N3$ are illustrated here. For more details see our recent arXiv contributions. $N2$ is time-reversible with its $N2^{-1} = T * N2 * T$, where the Time-Reversal Mapping T changes the sign of the vertical “momentum”, $T(q, \pm p) = (q, \mp p)$. Although the two mappings are similar $N3$ is not time-reversible.

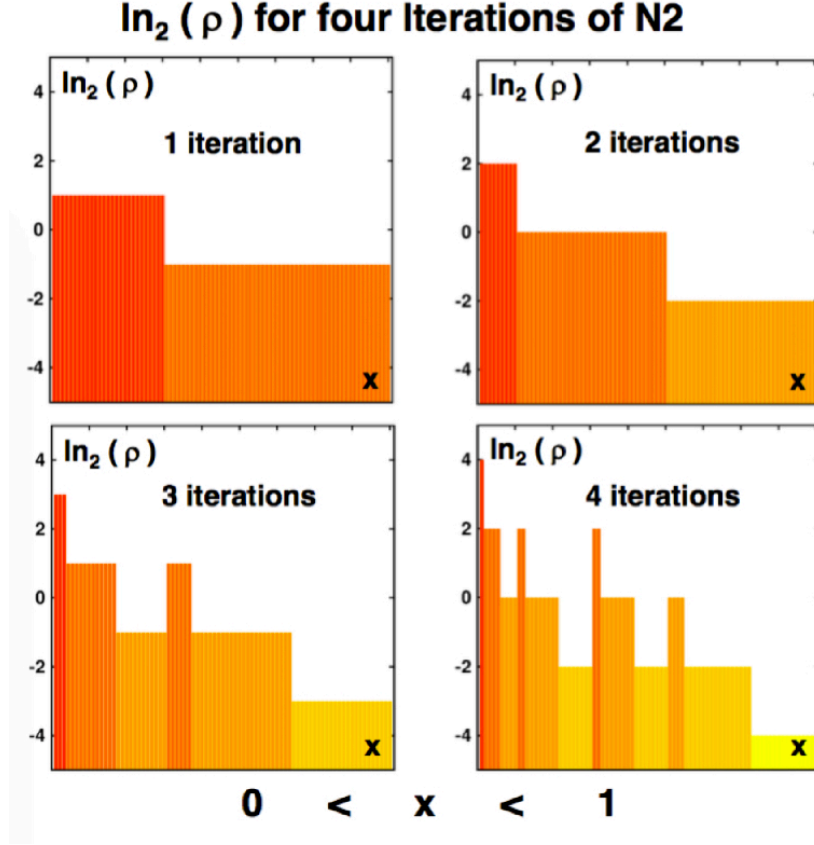


FIG. 7: The histograms resulting from four iterations of the random walk version of the N2 map in the unit square. The initial distribution of one million points was uniform in the unit interval ($0 < x < 1$). After the first iteration, with one third of the points moving left and two thirds right the probability density is 2 for ($0 < x < 1/3$) and $(1/2)$ for ($1/3 < x < 2/3$). Two iterations give probability densities of 4 for ($0 < x < 1/9$), 1 for ($1/9 < x < 5/9$) and $(1/4)$ for ($5/9 < x < 1$). After the fourth iteration the numbers of bins at each level of probability density, from the highest, 16, to the lowest, $1/16$, are $\{ 1 \times 1, 2 \times 4, 4 \times 6, 8 \times 4, 16 \times 1 \}$, 81 in all.

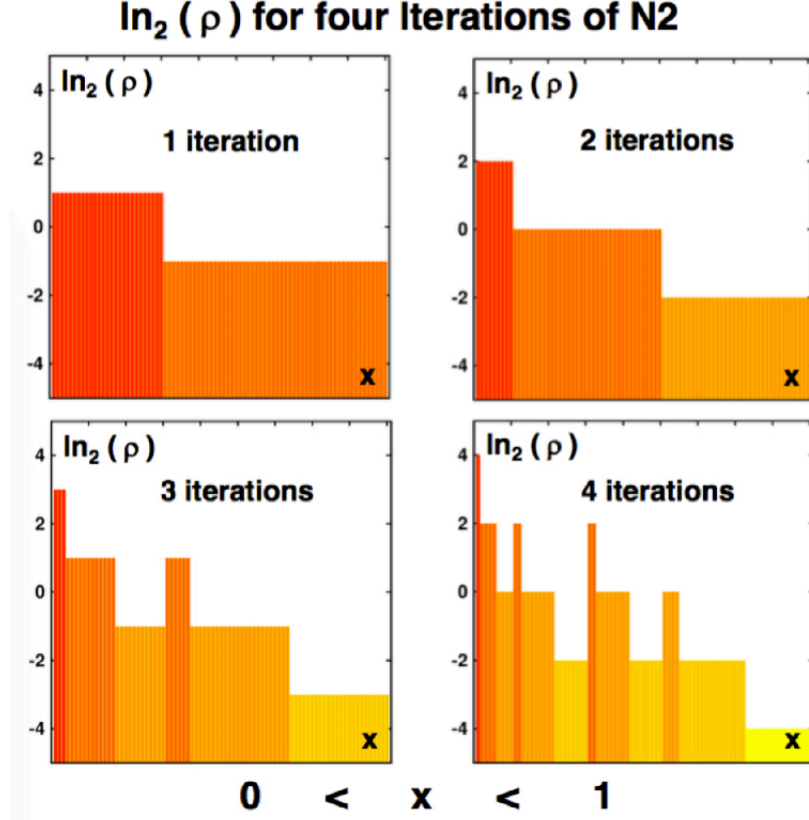


FIG. 8: The histograms resulting from four iterations of the random walk version of the N3 map in the unit square. The initial distribution of one million points was uniform in the horizontal interval ($0 < x < 1$). The histograms show the base-2 logarithms of the fraction of the points in each of 81 bins of equal width. These bin probabilities are equal here to probability densities which integrate to unity over the interval ($0 < x < 1$). We show five different probability-density levels from 2^4 for the highest probability density to 2^{-4} for the least probable. After the fourth iteration the numbers of bins at the five different levels, from the highest probability to the lowest, are exactly the same as those from the N2 mapping in **Figure 7**.

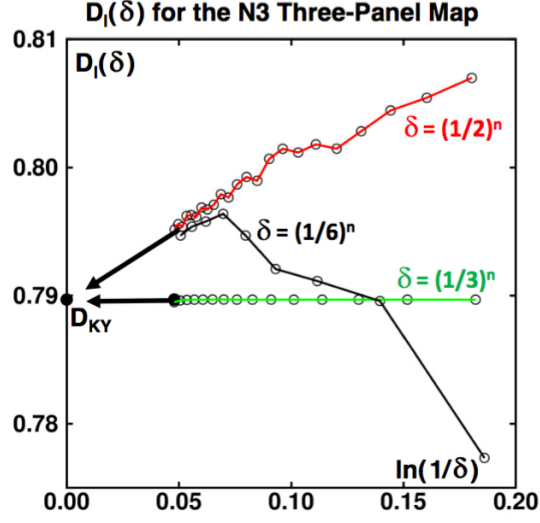


FIG. 9: Information Dimension data for the random walk problem equivalent to the N3 Mapping are all consistent with the same information dimension $D_I = D_{KY} = 0.789690$ for the Walk and 1.789690 for the Mapping. Pointwise analyses of the N3 mapping are described here for meshes of $(1/2)^n$ (red), $(1/3)^n$ (green), and $(1/6)^n$ (black). Analogous data for the N2 mapping are displayed in Figure 5 of Reference 18.